System design study of a VLEO satellite platform using the IRS RF helicon-based plasma thruster

11 January 2025

System design study of a VLEO satellite platform using the IRS RF Helicon-based Plasma Thruster

G. Herdrich[a]*, K. Papavramidis[a], P. Maier[a], J. Skalden[a], F. Hild[a], J. Beyer[a], M. Pfeiffer[a], M. Fugmann[a], S. Klinker[a], S. Fasoulas[a], N. Souhair[b], F. Ponti[b], M. Walther[c], A. Wiegand[c], L. Walpot[d], B. Duesmann[d], E. B. Borras[d], P.C.E. Roberts[e], N.H. Crisp[e]

[a] *Institute of Space Systems, University of Stuttgart, Pfaffenwaldring 29, 70569 Stuttgart, Germany,* herdrich@irs.uni-stuttgart.de
[b] *Alma Propulsion Laboratory, Department of Industrial Engineering, University of Bologna, Forli 47122, Italy*
[c] *Astos Solutions GmbH, Meitnerstr. 8, 70563 Stuttgart, Germany*
[d] *ESA – European Space Agency, ESTEC, Noordwijk, the Netherlands*
[e] *The University of Manchester, Manchester, George Begg Building, Sackville Street, Manchester, M13 9PL, UK*

* Corresponding Author

Abstract

To achieve a feasible lifetime of several years, most satellites are deployed in orbits higher than 400 km. Drag of residual atmosphere causes a slow orbit decay, resulting in the deorbit of the spacecraft. However, e.g. optical instruments or communication devices would significantly benefit from lower altitudes in the range of 150-250 km. A solution to achieve this could be the application of atmosphere-breathing electric propulsion (ABEP), where the residual atmosphere is used to generate continuous thrust that compensates the drag.

Within the EU-funded DISCOVERER project, the Institute of Space Systems (IRS) developed an electrode-less RF Helicon-based Plasma Thruster (IPT) suitable for such applications. Ignition and preliminary discharge characterizations of the IPT have been carried out at IRS facilities, using argon, nitrogen and oxygen. To further characterize the plasma plume, a torsional pendulum has been designed to determine the (local) momentum flux in the plasma jet, as well as a three-axis magnetic B-dot probe to carry out time-varying magnetic field measurements. Various intake designs were investigated, opening the possibility to conduct studies on potential satellite platforms within the frame of the ESA-funded project RAM-CLEP.

A design study for an Earth Observation and Telecommunication satellite operating at 150-250 km with an extended mission lifetime is currently being carried out. The first system assessment focused on the comparison of different spacecraft configurations ("slender body" and "flat body") and intake designs (specular or diffuse) with regard to overall drag and ABEP performance requirements.

In this contribution, the design approaches for the current thruster and the diagnostic methods are depicted. Moreover, the current status of the system assessment is presented. Upcoming experimental studies of the ABEP system e.g. within the ESA-project RAM-CLEP and additional activities planned on system assessment are outlined.

Keywords: very low Earth orbit, atmosphere-breathing electric propulsion, inductive plasma thruster, platform design

Nomenclature

C_D	=	Drag coefficient
I_{SP}	=	Weight-specific impulse
η_c	=	Intake efficiency
η_T	=	Thruster efficiency

Acronyms/Abbreviations

ABEP	Atmosphere Breathing Electric Propulsion
DSMC	Direct Simulation Monte Carlo
ESC	Electrostatic Comb
HOPG	Highly Oriented Pyrolytic Graphite
IPT	Inductive Plasma Thruster
IRS	Institute of Space Systems
MFP	Momentum Flux Probe
PFG	Particle Flow Generator
RF	Radiofrequency
TRL	Technology Readiness Level
VLEO	Very Low Earth Orbit

1. Introduction

To achieve a feasible lifetime of several years, most satellites are usually deployed in orbits higher than 400 km. However, very low Earth orbits (VLEO) can open up various new missions and benefit optical instruments and communication devices in the range of 150-250 km [1,2]. The challenge of these missions is the residual atmosphere that acts as a drag source in VLEO. A system that can utilize the atmosphere's particles as propellant to produce thrust can maintain the orbit, achieving a higher lifetime without the need for a

propellant tank. Both academia and industry are currently developing solutions for this application [3–15]. Within the EU H2020 DISCOVERER project [16], the RF helicon-based plasma thruster (IPT) [17–19] was commissioned and set in operation as well as various atmospheric intakes [18,19] were investigated and developed at the Institute of Space Systems (IRS) of the University of Stuttgart. These developments form the basis of a system study on a long-lived VLEO satellite platform suitable for Earth observation [20] and telecommunication applications [21] currently carried out under the ESA-funded RAM-CLEP project. Systems based on Atmosphere-Breathing Electric Propulsion (ABEP) technology can enable such missions and beneficially contribute to them. Possibly, in-space security applications may be able to be covered by such systems as well [22,23].

An ABEP system consists mainly of two elements: the intake (or mass collector) and the electric thruster, as shown in Fig. 1. Such systems have two basic functions: a) collecting the residual particles of the atmosphere via the intake and b) feeding those particles to the thruster as propellant for ionizing and accelerating them using radio-frequency (RF) waves and electromagnetic (EM) fields. The resulting plasma plume is quasi-neutral eliminating the need of a neutralizer. The overall underlying mechanism to produce the required thrust to compensate the drag is achieved in an electrode-less manner, enabling a maximum propellant flexibility in terms of composition and density as well as system compatibility with aggressive gases, such as atomic oxygen.

The present work is divided into three main parts. The first part is focused on the characterization activities of the thruster (IPT) performance in terms of thrust, as well as the detection of helicon waves in the plume [24,25]. To measure the thrust, a torsional pendulum was developed and the advanced design with preliminary measurements is presented in this paper. In addition, a magnetic inductive B-dot probe set-up and its calibration activities are described and discussed within this work, aiming to confirm the IPT as a helicon wave source. However, verifying investigations in [26] already imply the presence of Helicon modes in comparable systems. The second part shortly introduces two different kinds of atmospheric intakes that are considered within this study and presents recently identified limitations on the intake design. The third part presents the results of the system study on the proposed VLEO platforms. It starts with an introduction on the different spacecraft configurations considered. Supported representative payloads are outlined and the resulting requirements on the platform design are discussed. Finally, the methodology to calculate the spacecraft drag for the different configurations is described and a comparison of the resulting performance needed by an ABEP system is shown. It concludes with a description of the impact that the identified intake design limitation has on the overall system.
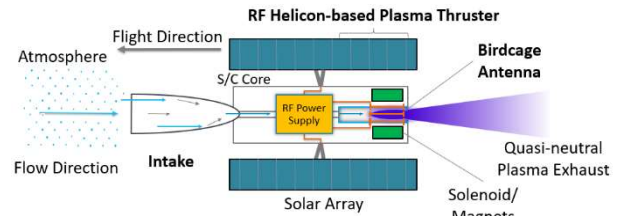

Figure 1. ABEP system schematic reworked from [17].

2. RF Helicon-based Plasma Thruster Design and Testing Activities

2.1 IRS RF Helicon-based Plasma Thruster Design

The RF Helicon-based Plasma Thruster (IPT) has been designed, developed, and successfully tested with argon, nitrogen and oxygen as propellants at IRS [17,18]. In Fig. 2, a schematic of the IPT is shown, featuring all the main components of the thruster: propellant injector (used also as frequency fine-tuning mechanism), discharge channel, birdcage antenna, Faraday shield, external solenoid (DC magnet), and support structure(s). The developed laboratory model [19], seen in Fig. 3, is attached externally to the vacuum chamber.
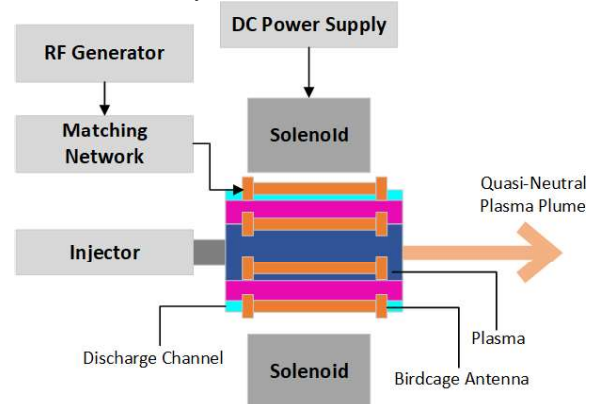

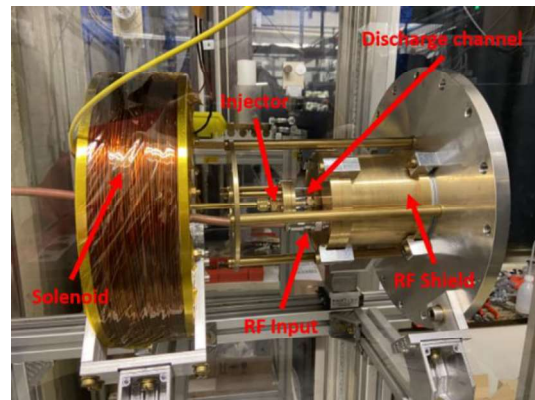Figure 2. Laboratory IPT schematic [18].

Figure 3. IPT lab model with solenoid on the left [19].

The current IPT features a novel RF antenna, called birdcage antenna, operating at 40.68 MHz. It is a directive antenna, fostering an $\vec{E}x\vec{B}$ velocity component to the charged particles [19]. Its discharge channel has an inner diameter of 37 mm. The external solenoid can produce a magnetic field up to 70 mT at a current of 15 A. The Faraday shield acts as an isolation of the EM fields by the antenna with the ambient environment. So far, the thruster is operated at input powers of 50-150 W, with a maximum of 300 W continuously tested. The detailed design and the operational envelope of the IPT is discussed in [17–19].

2.2 Momentum Flux Probe Design

The newly developed momentum flux probe (MFP) can be considered as a means to measure the IPT performance. By placing the probe in the plasma plume, radial and axial mapping can be conducted, extracting thrust information indirectly by measuring the momentum flux. This method provides the necessary information to assess if the thrust history is axially symmetric. Total thrust values are deducted by integrating the radial momentum flux recordings from a dedicated axial distance. By comparing the overall design with existing helicon thruster performances, a thrust range of around 1 mN is to be expected, an information, that has then served as major design driver for the pendulum [27,28]. The selected probe type is a torsional pendulum using a baffle plate, featuring neglectable gravity influence when balanced properly. Its baffle plate currently has a diameter of 20 mm. However, this diameter can also be varied in order to e.g. consider higher requirements referring to the radial resolution of the set-up.

The MFP consists of two main subsystems: the support structure and the pendulum itself. The support structure is connected to the test facility and hosts the pendulum. A frictionless flexural pivot bearing connects the pendulum with the support structure limiting dynamics to movement about the z-axis. Displacement is measured with an LED sensor pointing at an alumina target. Both a tilt sensor and the screws on the MFP base are used to adjust the tilt. Moreover, rubber feet are incorporated in the design to counteract any vibrations coming from the facility, optimized for the vacuum pump frequency. Aluminium is mainly used to avoid any influence on the discharge region due to magnetism [29]. The pendulum arm has an asymmetric L-shape design to facilitate the movement of the probe and to keep the other parts in adequate distance from the plasma plume. Furthermore, this allows to bring the probe close to the thruster's exit plane. The shaft is mounted on the arm's beam. The baffle plate is made of graphite due to high ion absorption rate and low sputter yield [30]. It is electrically isolated from the pendulum, to quickly adapt to the plasma potential in the plume in order to avoid

electrostatic forces. Such a design requires balancing and hence a counterweight and balancing mounts were added on the pendulum to adjust the centre of gravity after assembling. This keeps the design flexible e.g. for the case of a needed target change. The MFP design is also discussed in [31] and [32].

The graphite target is 20 mm in diameter with a thickness of 5 mm. The probe assembly is shown in Fig. 4. A shield is used to protect all other parts but the target, which is in direct contact with the plasma, see Fig. 5. This is done to mitigate parasitic displacement by other parts as well as reducing influence on the plume itself. In addition, a 10 cm distance between the target and the shield is maintained to minimize any flow reflection.

2.3 Momentum Flux Measurements

To calibrate the MFP, an electrostatic comb (ESC) is used to compare displacement against a known force. The ESC is a two-metal part where a voltage is applied, creating an attracting force. This force is independent of the exact distance between the plates and it is proportional to V^2 [33]. The expected force on the target, using the 20 mm graphite plate is estimated at the range of µN as mentioned before, assuming a symmetric and homogenous plume [27,32]. Hence, the MFP needs to detect values in this range as well as one or two orders of magnitude smaller, depending on the distance from the IPT exit plane.
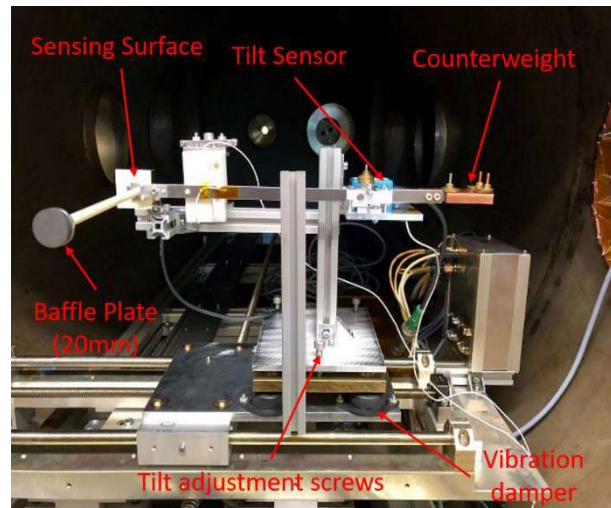
Figure 4. Momentum Flux Probe assembly with electrostatic comb for calibration and sensors [32].

The calibration process consists of two main steps. First step is to calibrate the ESC before mounting it on the pendulum and the second step is to calibrate the arm with the ESC mounted. The set-up for the ESC calibration is shown in Fig. 6. The set-up uses a Shimadzu AUW220D precision balance with 3D-printed base to elevate the ESC. One part of the ESC is mounted

on this base while the other part is mounted on a lid placed on top. At this distance, no interference between the balance's electronics and the comparably high voltage applied on the ESC was measured. Different measurement sets were recorded in order to extract a calibration curve (see Fig. 8).

A linear behaviour, as expected, is shown from the recorded measurements. A linear fit line is used to match the expected linearity of the force with respect to V^2. Five different measurement sets were conducted and for each voltage point the measurement was repeated three times. The results show repeatability among the different datasets, showing a linear trend between force and V^2. The measurement range applied was 0–1000 V, resulting to forces of 0–0.9 mN.
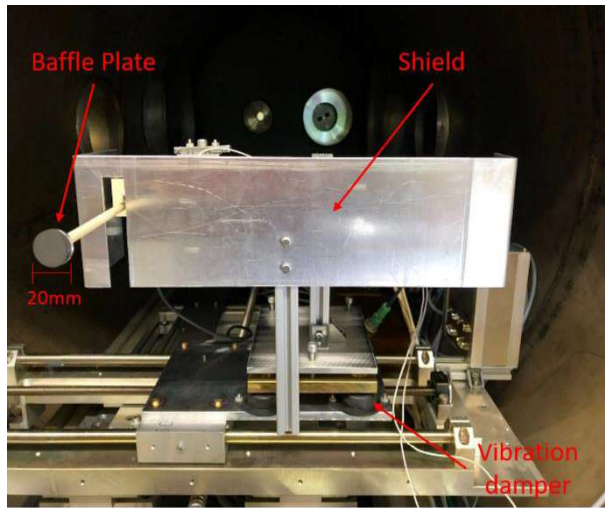

Figure 5. MFP with shield as protection from the plasma plume mounted in test facility Tank 12 at IRS [32].
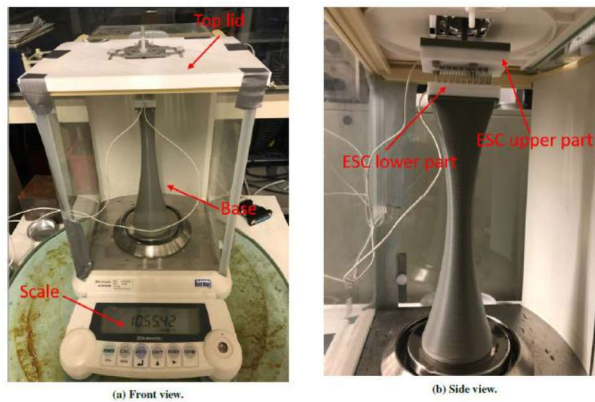

Figure 6. ESC calibration set-up [32].
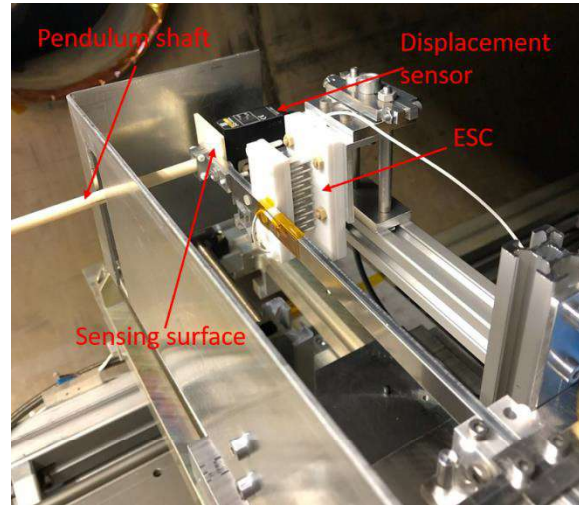
Figure 7. MFP calibration set-up with ESC mounted on the pendulum [32].

Next step in the calibration process is the mounting of the ESC on the pendulum and the support structure as shown in Fig. 7. The calibration of the pendulum is performed in vacuum conditions. The relation between voltage and displacement of the arm is extracted. After the stabilization of the pressure inside the chamber, the aforementioned voltage range is applied to the ESC and the LED displacement sensor data are recorded. By translating the displacement data into force, the results are plotted in Fig. 9. A fitting line in the data shows the linear behaviour of the results. This step concludes the construction of the final calibration curve as well as closes the calibration process. Then, the set-up is prepared to conduct momentum flux measurements on the IPT.

Figure 8. ESC calibration results and fitting curve of the measurement data using a precision balance.

Figure 9. Pendulum calibration results and fitting curve with the ESC mounted.

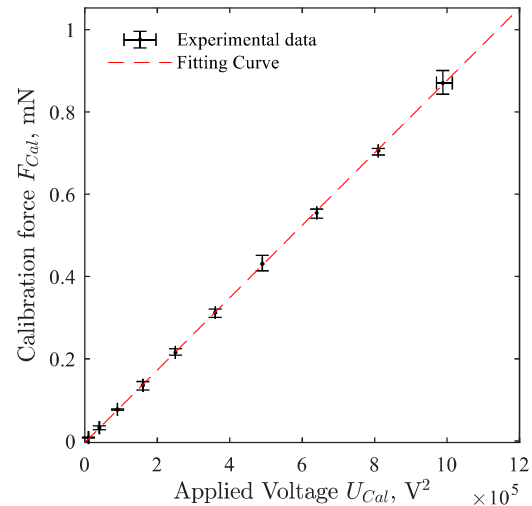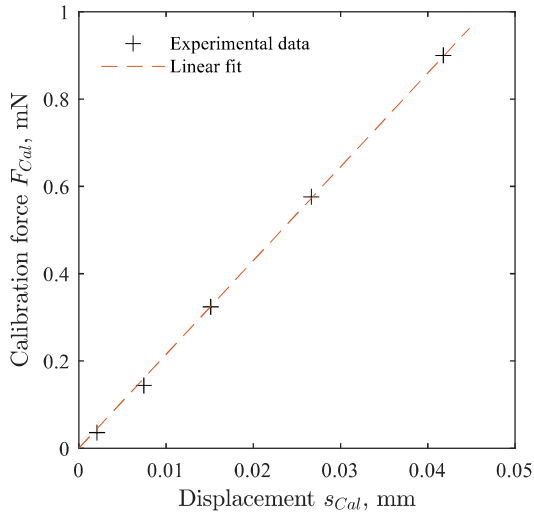To assess thermal influence on the probe, PT100 resistance temperature detectors were positioned where LED and tilt sensors are installed and in front of the shield. During operation of the thruster, the temperature stabilized at 25 °C, hence, no significant thermal drift is to be expected. After mounting the LED and tilt sensors on the MFP, the IPT was used under different conditions to check the functionality of the probe. It was operated under two modes: IPT operated using only cold gas flow (i.e. IPT power off) and IPT ignited (i.e. IPT power on). Different mass flows and power levels were applied during the test activities, monitoring the behaviour of the MFP. Movement of the MFP, which is correlated to thrust, during the cold gas and the plasma flows was identified.

Preliminary measurements were conducted for a power range of 60-150 W and with a mass flow rate range of 20-600 µg/s of argon. For each mass flow rate level, the external magnetic field of the solenoid was respectively adjusted to trigger different operational modes. A stronger external magnetic field of 40 mT was applied at the start of each mass flow rate change to keep the reflected power in low levels. This is further described as uncollimated mode, as the plasma didn't show a collimated jet in the center. Reducing the magnetic field to 22-27 mT results in a collimated jet and increased brightness. This potentially marks the shift to helicon wave mode, however, confirmation via B-dot probe is required. This behavior is further described in [19]. The external magnetic field is then further reduced till peak collimation and brightness is reached at around 13 mT. This mode is referred to as collimated mode.

Figure 10 and Figure 11 display the obtained data from the measurement campaign. The uncertainty on the y-axis is conservatively set to 30%, since the momentum

flux probe was not fully characterized yet and plume mapping was not yet possible. Instead, derived thrust caused by inserting the 20 mm graphite baffle plate into center the plasma plume was extrapolated homogenously to cover the entire plume's cross-section. Since the actual momentum and velocity profile of the plume is unknown at the moment, this methodology is considered with the conservative uncertainty. Uncertainty of the mass flow rate is derived from the Bronkhorst FG-201CV flow controller specifications.

Data for mass flow rates in the range of 20-80 µg/s is displayed for uncollimated and collimated mode and for the two power levels 100 W and 150 W. On average, higher power levels result in elevated performance. Furthermore, the expected behavior of increased weight-specific impulse with lower mass flow rate can be seen. The collimated mode shows significantly higher performance values compared to the uncollimated mode, further underlining the assumption that the helicon wave mode is triggered.

For 150 W, the thrust efficiency reached up to 16%. If this value can be verified with a fully characterized momentum flux probe, it would prove the envisioned performance gains of the ExB drift. Furthermore, cross connections using alternative measurement techniques are currently in preparation. This will be done, for instance, using an interferometric force probe [34,35], which can spatially resolve the momentum transfer of charged particles, making a cross-comparison between the two probes. Additionally, the implementation of the B-dot probe, described next, can be used to extract data that can characterize the discharge of the thruster and cross-correlate with different performance modes.
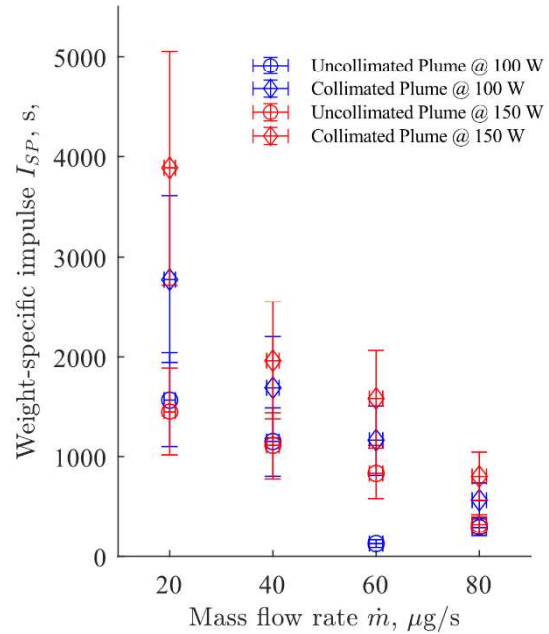

Figure 10: Weight-specific impulse over mass flow rate
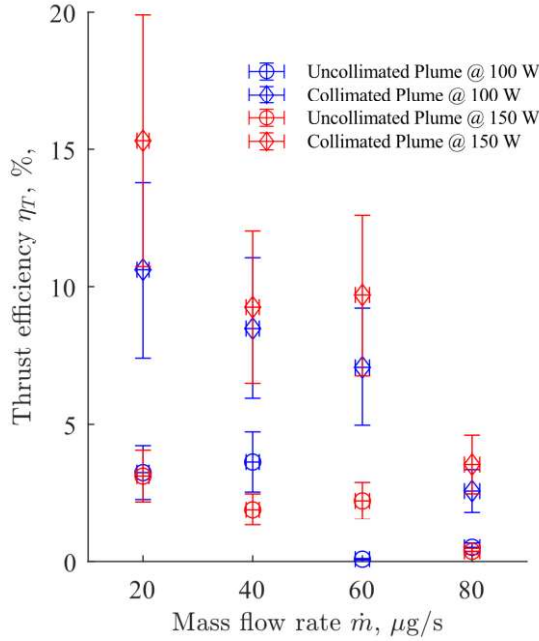
for different power levels and plume mode.

Figure 11: Thrust efficiency over mass flow rate for different power levels and plume mode.

Follow-on test activities of interest are going to be measurements placing the probe at different distances from the plasma plume to investigate its potential influence in the IPT discharge behaviour. Also, the potential reflection disturbances of the shield on the pendulum will be examined. Furthermore, plume mapping at different distances from the thrust shall provide information about the plume divergence and homogeneity of thrust. The latter is a crucial parameter for the ongoing ABEP platform development.

2.4 Inductive Magnetic B-dot Probe Set-up

An inductive magnetic B-dot probe has been developed and built to investigate on the IPT discharge behaviour [19]. This type of probe is used to detect the rotating magnetic field of the helicon waves inside the plasma plume. The operational principle of the B-dot probe is governed by Faraday's law of induction, shown in Eq. 1, where ϵ is the electromotive force and ϕ_B is the magnetic flux.

$$\epsilon = -\frac{d\phi_B}{dt} \qquad (1)$$

A conductive wire loop is the sensing element of the probe. Three coils are used to get measurements in three directions. In Eq. 2, the magnetic field induces a voltage on the coils, which is used to estimate the amplitude of the B-field [24,36,37]. The NA is the calibration factor where N is the number of loops, A is the area enclosed by the loop and ω is the angular frequency.

$$V = -NA\left|\frac{dB_{tot}}{dt}\right| = -NA\omega|B| \qquad (2)$$

The working frequency of the IPT is at 40.68 MHz and the maximum loops for each coil is chosen equal to N=5. PEEK is mostly used for the probe. A borosilicate glass tube encloses the probe to minimize contact with the plasma. The design layout is depicted in Fig. 10. The sensing signal on the coils passes through the cabling inside the tube, ending up in an RF power combiner for each axis to remove the capacitive pick-up voltage that arises between coils and plasma. The measurements are recorded using an oscilloscope.
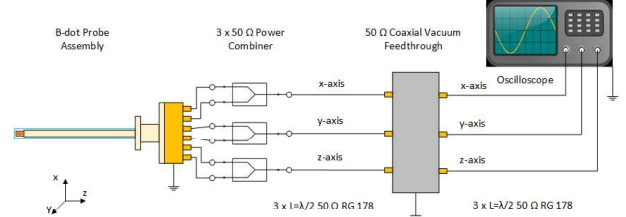
Figure 10. B-dot probe schematic [18].

Two set-ups were developed to calibrate the probe over a broad range of frequencies. For what concerns low frequencies, a Helmholtz coil is used [36,38]. The set-up is shown in Fig. 11 while the circuit schematic is based on [38]. Each coil is made of N=27 loops with a copper wire of 1 mm in diameter. The coils are mounted on a PA base. Each coil has a diameter of 104 mm and the distance between them is 55 mm. The base and probe are mounted on 3D-printed parts to facilitate the alignment.
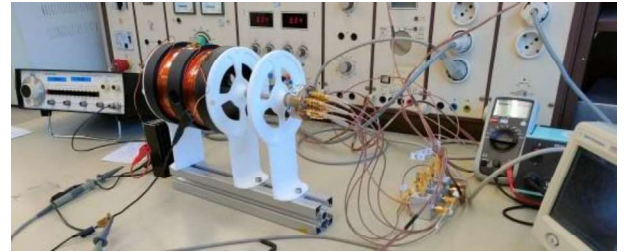
Figure 11. Helmholtz coil set-up for low frequency calibration of the B-dot probe.
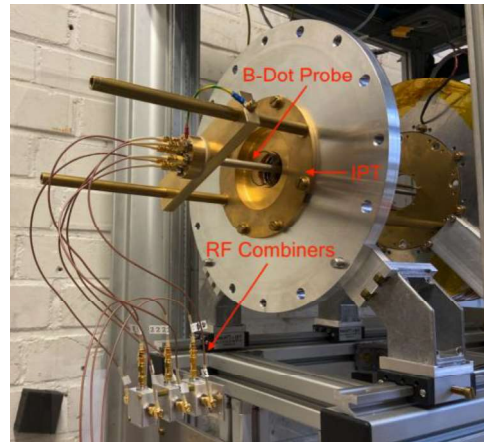
Figure 12. B-dot probe high frequency calibration set-up [19].

High frequency calibration uses the IPT itself which is described in reference [24]. The calibration process in this case employs the homogeneous and linearly polarized magnetic field inside the thruster. The set-up is shown in Fig. 12. Different voltages at the resonant frequency are given to IPT via a function generator and the output signal is recorded with an oscilloscope. The rotating magnetic field can be reconstructed with further data post-processing and analysis of the measurements. The calibration of the probe is currently undergoing and will be followed by the measurements in the plasma plume.

3. Atmospheric Intake Designs

In addition to the thruster, different designs for atmospheric intakes (or mass collectors), based on diffusely and specularly reflecting surface materials, have been studied at the IRS [39,40] and are considered for the spacecraft system study within this paper. These designs and further investigations on their limitations are shortly described in the following sections.

3.1 Intake Concepts and Early Simulations

The intake needs to efficiently collect atmospheric particles in a free molecular flow regime and guide them to the thruster's discharge channel. Different intake concepts have been proposed and studied for this purpose (see e.g. [39,40]), relying on different particle reflection properties of the intake material. In this paper, two intake types, based on diffuse and specular reflection of atmospheric particles, are considered.
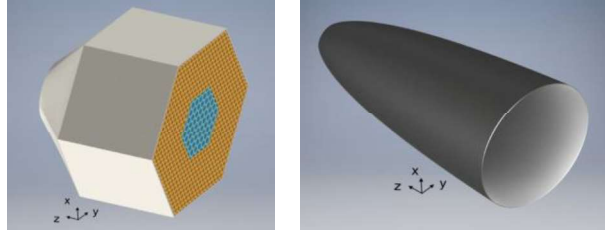

Figure 13. Diffuse (left) and specular (right) intake concepts [39].

The diffuse intake design (see Fig. 13, left) has a hexagonal shape and consists mainly of a straight section, followed by a converging section leading to the discharge channel. The front part of the straight section is made of small hexagonal ducts, acting as a particle trap, which increase the efficiency as well as the pressure.

The intake efficiencies of both designs were studied using Direct Simulation Monte Carlo (DSMC) simulations using the particle code PICLas [41]. For all intake simulations described in this paper atmospheric data from the NRLMSISE-00 model for the 15/02/2020 at 00:00:00 was used, corresponding to low solar activity

with a solar radio flux at a wavelength of 10.7 cm $F10.7 = 69.5$ and a geomagnetic index $Ap = 4.1$. This date was selected as it offered the latest updated solar activity data available from the NASA Community Coordinated Modeling Center at the time of the first simulation. It should be noted, however, that for more detailed design work, the atmospheric conditions should be reviewed based on the expected conditions during flight, as particularly the solar activity can lead to large variations in the atmospheric environment [31].

This diffuse intake design thereby showed intake efficiencies of η_c = 0.437-0.458 and mass flow rates entering the thruster of $\dot{m}_{thr}$ = 0.0212-0.0240 mg/s [39] (see Tab. 1 for details). A potentially suitable intake material featuring diffuse reflection of particles would be titanium or titanium alloys [13].

Table 1: Size and performance of diffuse intake used as design reference. Data from [39]

Altitude km	A_{intake} m²	η_c -	$\dot{m}_{thr}$ mg/s
150	0.008	0.456	0.0240
180	"	0.443	0.0053
200	"	0.445	0.0023
220	"	0.424	0.0011
250	"	0.416	0.0004

The diffuse intake design is relatively sensitive to misalignment of the incoming flow, with the efficiency dropping to η_c = 0.37 or less already at 5 deg misalignment between incoming flow and intake [39].

An improvement of the efficiency could be achieved by using materials that promise specular reflection characteristics, e.g. Highly Oriented Pyrolytic Graphite (HOPG) or Silicon Dioxide (SiO_2) [42]. This concept would not require ducts as particle traps. It would open up design options similar to those found in optical design, e.g. using parabolic shapes to collect the incoming particles at the focus point of the paraboloid (see Fig. 13, right). Early DSMC simulations showed this concept to be able to achieve an intake efficiency of up to η_c = 0.94, if the paraboloid focus point is placed inside the thruster's discharge channel (see Tab. 2 for details) [39].

Table 2: Size and performance of specular intake used as design reference. Data from [39].

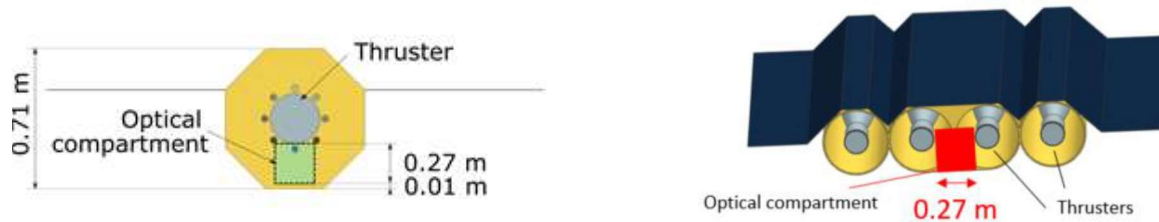| Altitude km	A_{intake} m²	l_{intake} m	η_c -	$\dot{m}_{thr}$ mg/s
150	0.019	0.258	0.943	0.232
180	"	"	0.934	0.052
200	"	"	0.930	0.023
220	"	"	0.926	0.011
250	"	"	0.922	0.004

Figure 14. Back views of the slender body (left) and flat body (right) configurations, indicating the placement of the Earth observation payload's optical compartment.

The specular intake is comparatively insensitive to flow misalignment, showing practically no efficiency loss up to 5 deg misalignment [39]. It is, however, considerably more sensitive to the material properties which may change due to material degradation over mission lifetime, e.g. caused by the exposure to atomic oxygen. DSMC simulations showed, however, that the efficiency remains above $\eta_c = 0.6$ for as long as the material provides at least 70 % specular reflection [39]. Additionally, the viable size range of the intake diameter of paraboloid intakes is practically limited by the allowable intake length (the length of the intake increases as a function of the square of the diameter, following the definition of the paraboloid; furthermore, the required location of the paraboloid's focus, determined by the diameter of the discharge channel has an influence). Assuming that the intake length is limited to approx. 3 m in order to fit into existing payload fairings, the maximum intake sizes as indicated in Tab. 5 result.

3.2 More Detailed DSMC Simulations of Specular Intakes and Identified Limitations

The abovementioned analyses of the specular intake designs all assumed idealized flow conditions in orbit, particularly assuming the thermal velocity component of the particles being zero. This simplification leads to the particles entering the intake as a nearly perfectly parallel flow, which also justified the parabolic design of the intake. More detailed DSMC simulations of the specular intakes with the particle code PICLas [33] showed, however, that the thermal velocity component of atmospheric particles in VLEO (300 to 1,900 m/s, depending on particle species and altitude/temperature) changes the direction of the relative velocity vector between intake and atmospheric particles significantly such that the particles cannot be assumed to enter the intake in parallel direction [43]. This inevitably leads to a decrease of the efficiency compared to the original expectations for paraboloid intakes, which are shape-optimized for parallel flows.

In order to identify consequential design limitations and to quantify the impact of the intake design and efficiency, several intake lengths of specular intakes, designed for thrusters with 15 mm and 37 mm discharge chamber diameter (see also Tab. 4) were investigated.

37 mm discharge chamber diameter thereby corresponds to the size of the current IPT. 15 mm discharge chamber diameter corresponds to an early design point of a more compact thruster. The first conclusion for the system design was that with the discharge chamber diameter being 15 mm, due to the particle's thermal velocity component and the slender shape of these intakes, sufficiently high intake efficiencies were not reachable even at small intake diameters (an intake with 0.16 m diameter would reach an efficiency of $\eta_c = 0.42$) [43].

Intakes designed for 37 mm discharge chamber diameter showed significantly higher intake efficiencies, but still not as good as the originally assumed 94 % (see Tab. 3). The simulations also showed a strong dependency of the intake efficiency on the intake length (or diameter) due to the thermal velocity of the particles. They clearly indicate that the original assumption that the intake efficiency can be treated as being independent of intake scaling cannot be maintained.

In order to illustrate the effect that the erroneous assumption of a parallel flow in the original simulations has on the system design – and to present a more realistic design – a design based on these identified limitations of the paraboloid specular intake is compared to designs based on the "original" intakes towards the end of this paper.

Table 3. Results of DSMC simulations considering thermal velocity of atmospheric particles for fully specular paraboloid intakes for a "large" thruster with 37 mm discharge chamber diameter (at around 200 km) [43]

Intake inlet diameter, m	0,42	0,36	0,3	0,2
Intake length, m	2	1,5	1	0,5
Intake area, m²	0,14	0,10	0,07	0,03
η_c, -	51%	60%	73%	90%

4. VLEO Spacecraft System Study
4.1 Considered ABEP System

The principle of the ABEP system as considered for the system study is shown in Fig. 1. It should be pointed out that within the scope of this paper, the ABEP system is considered to be integrated into the core of the spacecraft in a concentric manner, i.e. without complex

redirection or intermediate storage of the particles and with the rest of the system components located "around" the ABEP system(s).

For the purpose of this study, the operational mode is assumed to be continuous drag compensation by the ABEP system, i.e. thrust = drag. As such, the main performance parameters of the ABEP system can be considered to be:

- The intake efficiency η_c defined as the ratio of the collected particle flux in the thruster over the incoming particle flux at the intake frontal area;
- The thruster efficiency η_T;
- The achievable specific impulse of the thruster.

4.1.1 Thruster

The thruster considered for the system study is the IRS IPT described above. The advantages of this thruster type for an ABEP system include

- Its compatibility with atmospheric propellants,
- Its flexibility with regard to propellant density and composition,
- Its electrode-less nature (omitting problems with degradation of electrodes exposed to atomic oxygen flow)
- A quasi-neutral plasma plume (omitting the need for an additional neutralizer).

The laboratory model of this thruster has already been operated at powers slightly above 100 W, with expected thrust levels at the mN-level.

Based on laboratory measurements with a similar thruster type in reference [44], the thruster efficiency is currently estimated as $\eta_T = 20\%$ (even though the ExB drift is likely to lead to an improvement).

Detailed data on both thrust and thruster efficiency will be available from the ongoing momentum flux measurements.

Table 4. Main dimensions of considered thrusters

	Large thruster	Small thruster
Discharge channel diam.	37 mm	15 mm
Outer diameter	150 mm	150 mm
Length	300 mm	300 mm
Mass	2.07 kg	0.55 kg

In order to account for different thrust needs, in addition to the laboratory thruster described above (in the following referred to as "large" thruster), also a downscaled ("small") version, which is currently under development, is considered. The estimated geometric and mass envelopes for both thruster versions are indicated in Table 4Table 4 (the estimates are conservative and partly based on the laboratory device and partly on an improved design).

4.1.2 Intake Concepts

The intakes considered for the system study are the diffuse design and the paraboloid specular design as described in section **Error! Reference source not found.** above. As the paraboloid specular design is considered in combination with both "large" and "small" thrusters, two sizes of the specular intake are considered.

Table 5. Intake designs as considered for the system study. Intake design taking into account limitations of section 3.2 ("spec., limited") for comparison.

	Diff. intake	Specul., Large thruster	Specul., Small thruster	Specul., limited
Intake length	flexible	2.93 m	2.93 m	1 m
Intake inlet diam.	0.69 m	0.66 m	0.42 m	0.3 m
Single intake area A_{in}	0.39 m²	0.34 m²	0.14 m²	0.07 m²
Intake efficiency η_c	0.46	0.94	0.94	0.73

In addition, the aforementioned designs are compared to a paraboloid specular intake sized taking into account the performance limitations caused by the thermal movement of atmospheric particles as described in section 3.2. In this case, an intake length of 1 m was identified to provide a reasonable compromise between intake efficiency and collection area. The performance parameters of this intake are provided in Tab. 6

Table 6: Size and performance of "limited" specular intake as used within this study. Data from [43].

Altitude km	A_{intake} m²	l_{intake} m	η_c -	$\dot{m}_{thr}$ mg/s
150	0.0691	1.0	0.799	0.725
180	"	"	0.750	0.159
200	"	"	0.726	0.070
220	"	"	0.704	0.033
250	"	"	0.681	0.0121

4.1.3 Considered Spacecraft Configurations

ABEP satellite design is driven by the ratio of area of attack to intake area, affecting the drag, and required I_{SP} of the thruster. The challenge is to accommodate the payload, ABEP system, and other subsystem components in a way that results in a minimum frontal area. Two general spacecraft configurations have been developed and are examined in this paper, the slender body (left) and the flat body design (right) shown in Fig. 14. The former features a single ABEP system in the centre with satellite components arranged around it in an octagonal

spacecraft body, similar to GOCE's [45] design. The latter consists of an array of ABEP systems, placing all components in the slipstream of the intakes to reduce the area of attack. The flat body is capable of attitude control around one axis using the ABEP systems.

As the slender body configuration only foresees one thruster, the "large" thruster, either with a diffuse or a specular intake, is considered for this configuration. On the other hand, as the flat body configuration allows the use of several thrusters, the use of "small" thrusters is considered for this configuration. In this case, as section 4.2 will show, the payload can be positioned fully in the slipstream of specularly reflecting intakes. Diffuse intakes would not yield a higher ratio of intake area over frontal area (area of attack), but merely provide a lower intake efficiency. The flat body configuration therefore is only considered with specular intakes.
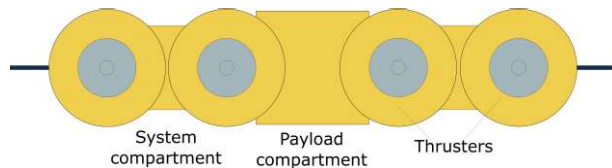

Figure 15. Sketch of flatbody adapted for specular intake with 0.3 m inlet diameter (back view).

The specular intake adapted to the limitations of section 3.2 unfortunately does not have a sufficiently large diameter that would allow payload and system components to be placed in the slipstream of the intake. For the analysis case with the adapted specular intake, the "flat body" configuration (Fig. 14, right) is therefore adapted to include three compartments for the payload and the system components in between the intakes and thrusters (see sketch in Fig. 15). The adapted flat body configuration is the only configuration that adapts drag-reduction measures. Due to its short and wide spacecraft body, part of the solar panels are assumed to be deployed behind the spacecraft body (see sketch in Fig. 16). As the particle flow only refills the "void" behind the spacecraft body under a certain refill angle, the nadir side of the backwards-deployed panels can be assumed to be "shadowed" from parallel flow and therefore to not contribute to drag (also see Table 17 and compare [46]). It should be noted that potential interactions between the thruster plumes and the solar panels have not been studied or taken into account, which may limit the drag-reducing effect.

4.2 Payload and Resulting Design Requirements on the System

The platform is designed to accommodate two payloads simultaneously: an Earth observation payload with about 20 cm aperture size, and a telecommunication payload with a close-to-hemispheric antenna. While the requirements on the overall spacecraft configuration posed by the telecommunication payload are minor, the Earth observation payload requires an optical payload compartment with a size of approximately 270 mm x 270 mm x 390 mm (H x W x L). All configurations are sized accordingly so that this payload compartment can be placed below the thruster (slender body) or in between the two centre thrusters (flat body), always in the slipstream of the spacecraft frontal surface, see Fig. 15.
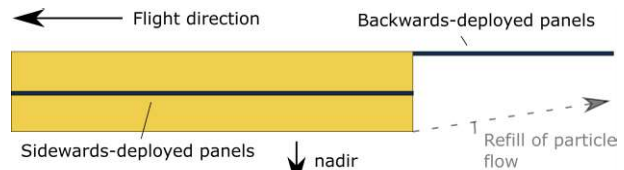

Figure 16. Sketch of adapted flatbody configuration with drag-reducing backward deployment of solar panels (side view)

For the slender body configuration, this implies that the diameter of the octagonal body has to be at least 0.71 m in order to place the optical compartment underneath the "large" thruster. Comparing this requirement with the size limitation of the specular intakes listed in Tab. 5, it becomes obvious that a specular intake in this case cannot "cover" the full frontal area at a feasible length. A full coverage in this case is only possible with a diffuse intake. For the flat body, coincidentally the largest possible diameter of specular intakes of 0.42 m would just allow the optical compartment to fit in between the two central intakes. Smaller intake diameters are possible, but would require the two central intakes to be moved further apart than mandated by their own diameter.

For the early concept assessment at hand, it is furthermore assumed that 10 m² of solar panels are required and sufficient to provide the payload, the ABEP system, and the rest of the spacecraft with power at the end of life. A more detailed assessment including a multi-dimensional optimization of the system design is currently being conducted in a next design step.

4.3 Spacecraft Drag

4.3.1 Methodology to Calculate Drag
One key to comparing the different spacecraft configurations for VLEO is the drag induced by the different shapes. In the flow domain encountered in VLEO, surfaces parallel to the flow also provide a significant contribution to total drag. Only using a single literature-based drag coefficient in combination with the spacecraft frontal area is therefore not suitable for comparing spacecraft shapes. Furthermore, as drag reduction becomes relevant, the spacecraft will tend to deviate from the "box" shape often encountered in higher

LEOs. The often-cited value of $C_D = 2.2$ will therefore in most cases not be appropriate for a VLEO spacecraft. The measured drag coefficient of $C_D = 3.7$ for GOCE confirms this tendency [47].

A detailed drag analysis, however, would require time-consuming DSMC simulations. This would slow down an early concept analysis considerably and, given time constraints, reduce the concept space that can be analysed.

An additional problem, that often gets ignored, specifically applies to ABEP systems: how to take into account the drag contribution of the ABEP system (particularly the intake) itself. Past VLEO system studies often merely added the intake area to the rest of the frontal area of the spacecraft when calculating drag based on C_D, not making any distinction [2,39,48,49].

In this analysis, the first challenge is solved by assuming – as a very first iteration step – that all surfaces of the spacecraft geometric model are either parallel or perpendicular to the flow. This simplification allows a straightforward analytical analysis of different general configurations following a "panel method" approach, using Eq. 3 to calculate the total spacecraft C_D:

$$C_D = \frac{A_{\parallel} \, C_{D,\parallel} + A_{\perp} \, C_{D,\perp}}{A_{ref}} \qquad (3)$$

Where $A_{\parallel}$ is the surface area of spacecraft oriented parallel to the flow, $A_{\perp}$ is the surface area of the spacecraft oriented perpendicular to the flow, $C_{D,\parallel}$ is the (area-specific) drag coefficient of areas parallel to the flow, $C_{D,\perp}$ is the (area-specific) drag coefficient of areas perpendicular to the flow, and A_{ref} is a reference area (we use the spacecraft cross-sectional area, which corresponds to the full frontal area $A_{frontal}$ for both configurations). The altitude-dependent, area-specific drag coefficients for parallel and perpendicular surfaces are calculated using the Sentman model for gas-surface interactions [50], assuming an energy accommodation coefficient of 1 and a wall temperature of 300 K. The resulting values are plotted in Fig. 17.
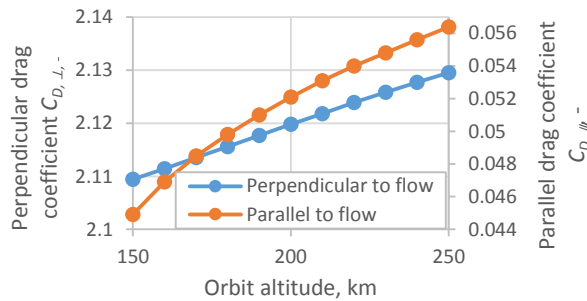

Figure 17. Area-specific drag coefficient C_D according to the Sentman model for different altitudes as used for the calculation of drag.

In order to verify this simplified model, comparisons were carried out for slender body and flat body geometries with the more advanced panel-method-based tool ADBSat [51] and DSMC simulations in PICLas. All comparisons yielded differences of less than 2 % in the obtained drag coefficient for the full spacecraft.

While this method is quite limited in the geometries that can be analysed, it provides the opportunity to quickly make comparisons of basic configuration options and to widen the analysis space.

The second challenge, the contribution of the intakes to drag, is, due to the geometry of the intakes as well as the potential influence of the engines, not as straightforward to solve without DSMC simulations. Efforts in this direction are currently ongoing at the IRS for specular intakes in particular. Naively, one would expect that they do contribute to drag, but much less than a solid, perpendicular surface of the same size. For the scope of this paper, therefore a broad approach was taken, assuming that the intakes produce some unknown fraction β of the drag that a solid surface, perpendicular to the flow, with the same size as their frontal area would produce. All configuration options were then analysed over the full range of possibilities: from the assumption that the intakes do not contribute to drag at all ($\beta = 0$) to the assumption that the intakes contribute to drag like a solid, perpendicular surface the same size as their frontal area would ($\beta = 1$). This allows to account for the drag induced by the intakes as formulated in Eq. 4.

$$F_{D,intakes} = 0.5 \, \rho \, (A_{intake} \, C_{D,\perp} \beta) \, v^2 \qquad (4)$$

Here, A_{intake} is the frontal area of the intake, ρ is the atmospheric density, and v is the spacecraft velocity relative to the atmospheric gas.

4.3.2 Estimated Drag

As a first step of comparison, drag coefficients and drag are compared for three basic configurations: the slender body with a diffuse intake (covering the full-frontal area, except necessary structure), the slender body with a specular intake (of only 0.66 m diameter, see section 2.2), and the flat body with specular intakes (covering the full-frontal area, expect necessary structure and central compartment).

For each configuration, the impact of certain modifications is shown. As reference area to calculate C_D, always the *full* cross-sectional area of the spacecraft (including the area covered by the intakes) is used.

Concluding the section, drag coefficients and drag are also shown for the "adapted" flat body that considers the limitations on specular intake design posed by the thermal movement of atmospheric particles.

4.3.2.1 Slender Body with Diffuse Intake

For the slender body with a diffuse intake, the geometric dimensions as listed in Tab. 7 are used. The configuration layout is shown in Fig. 14, left.

Table 7. Geometric dimensions of slender body configuration with diffuse intake

Spacecraft length	3.2 m
Spacecraft (octagon) height	0.71 m
Spacecraft (octagon) width	0.71 m
Deployable solar panel width (each side)	1.21 m
Deployable solar panel thickness	0.01 m
Diffuse intake (octagon) diameter	0.69 m
Full frontal area	0.44 m²
Intake inlet area	0.39 m²

For a flight altitude of 200 km, the drag coefficient of this configuration was found to be 4.83 if the intake is assumed to be fully contributing to drag ($\beta = 1$) and 2.94 if the intake did not contribute to drag at all ($\beta = 0$). See also Tab. 8. Reality will likely lay somewhere in between.

Table 8. C_D of baseline slender body with diffuse intake, for a flight altitude of 200 km

	Intake fully contributing	Intake not contributing
C_D	4.83	2.94
Reference area	0.44 m²	0.44 m²

As Fig. 18 shows, the obtained C_D value varies slightly over the analysed altitude range, as the area-specific drag coefficients according to the Sentman model are a function of altitude.
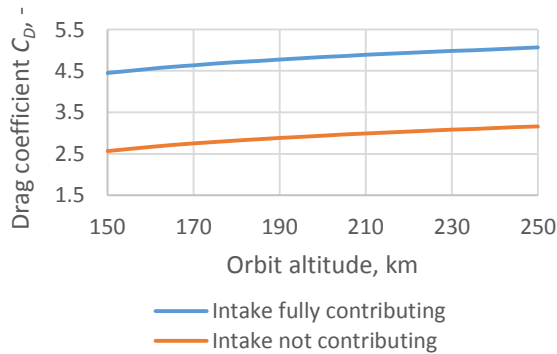

Figure 18. Variation of drag coefficient C_D over altitude for a slender body configuration with a diffuse intake.

Tab. 9 summarizes the resulting drag force at three exemplary altitudes that has to be compensated by the ABEP system for orbit maintenance. As the numbers show, the surfaces oriented parallel to the flow also contribute significantly to the total drag. The real drag to be expected will again be somewhere in between the values obtained for $\beta = 1$ and $\beta = 0$.

Table 9. Spacecraft drag at different altitudes for slender body with diffuse intake. $F_{D,\perp}$ and $F_{D,\parallel}$ denote drag contributions from surfaces perpendicular and parallel to the flow, respectively.

	150 km	200 km	250 km
	Intake fully contributing ($\beta = 1$)		
Total drag	124.0 mN	18.0 mN	4.8 mN
$F_{D,\perp}$	58.8 mN	7.9 mN	2.0 mN
$F_{D,\parallel}$	65.2 mN	10.1 mN	2.8 mN
	Intake not contributing ($\beta = 0$)		
Total drag	71.5 mN	10.9 mN	3.0 mN
$F_{D,\perp}$	6.3 mN	0.8 mN	0.2 mN
$F_{D,\parallel}$	65.2 mN	10.1 mN	2.8 mN

4.3.2.2 Slender Body with Specular Intake

The slender body with a specular intake resembles the slender body with a diffuse intake, besides the fact that the intake is smaller (length-limited) and therefore does not cover the full frontal area. Tab. 10 therefore only lists the intake-related dimensions.

Table 10. Intake-related geometric parameters of slender body with specular intake. All other parameters are the same as in Tab. 7.

Specular intake (circular) diameter	0.66 m
Full frontal area	0.44 m²
Intake area	0.34 m²

Consequently, the drag induced by the slender body with a diffuse intake equals that of the slender body with a specular intake, in case of $\beta = 1$ (compare also Tab. 9 and Tab. 12). Only for $\beta = 0$, the drag induced in case of the specular intake configuration is higher than in case of the diffuse intake configuration (see also Tab. 12 for different altitudes).

Table 11. C_D of baseline slender body with specular intake, for a flight altitude of 200 km

	Intake fully contributing	Intake not contributing
C_D	4.83	3.19
Reference area	0.44 m²	0.44 m²

Table 12. Spacecraft drag at different altitudes for slender body with specular intake. Values for $\beta = 1$ are the same as for slender body with diffuse intake.

	150 km	200 km	250 km
	Intake not contributing ($\beta = 0$)		
Total drag	78.4 mN	11.9 mN	3.3 mN
$F_{D,\perp}$	13.2 mN	1.8 mN	0.5 mN
$F_{D,\parallel}$	65.2 mN	10.1 mN	2.8 mN

4.3.2.3 Flat Body with Specular Intake

For the initial configuration of a flat body with specular intakes – with four intakes – the geometric dimensions are listed in Tab. 13. The configuration layout is shown in Fig. 14, right.

Table 13. Geometric dimensions of flat body with specular intakes

Number of intakes	4
Spacecraft length	3.4 m
Spacecraft height	0.44 m
Central body width	1.73 m
Deployable solar panel width (each side)	0.6 m
Deployable solar panel thickness	0.01 m
Specular intake diameter	0.42 m
Full frontal area	0.66 m²
Intake inlet area	0.55 m²

For a flight altitude of 200 km, the drag coefficient of this configuration was found to be slightly lower than for the slender body, i.e. 4.02 if the intake is assumed to be fully contributing to drag ($\beta = 1$) and 2.23, if the intake did not contribute to drag at all ($\beta = 0$), see also Tab. 14. Reality will likely again lay somewhere in between. Generally, however, it can be noted that there are no large differences between the drag coefficients of the two configurations (as also the plot over altitude for the flat body configuration in Fig. 19 confirms).

Table 14. C_D of baseline flat body with specular intake, for flight altitude of 200 km

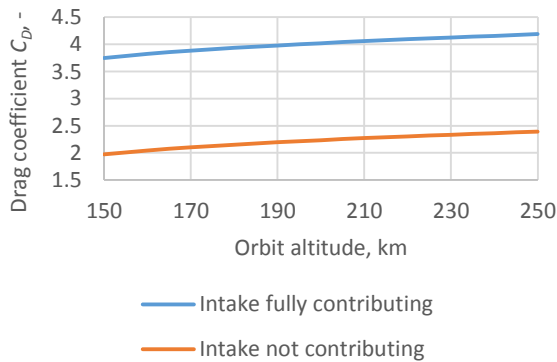|	Intake fully contributing	Intake not contributing
C_D	4.02	2.23
Reference area	0.66 m²	0.66 m²

Figure 19. Variation of drag coefficient C_D over altitude for a flat body configuration with a specular intake.

Tab. 15 again summarizes the resulting drag force at three exemplary altitudes for the flat body configuration. As the reference area (= frontal area) of the flat body configuration is larger than that of the slender body configuration, the resulting drag is higher, even though the drag coefficients are similar (or smaller).

Table 15. Spacecraft drag at different altitudes for flat body with specular intake. $F_{D,\perp}$ and $F_{D,\parallel}$ denote drag contributions from surfaces perpendicular and parallel to the flow, respectively.

	150 km	200 km	250 km
	Intake fully contributing ($\beta = 1$)		
Total drag	156 mN	22 mN	6 mN
$F_{D,\perp}$	88 mN	12 mN	3 mN
$F_{D,\parallel}$	68 mN	10 mN	3 mN
	Intake not contributing ($\beta = 0$)		
Total drag	82 mN	12 mN	3 mN
$F_{D,\perp}$	14 mN	2 mN	0 mN
$F_{D,\parallel}$	68 mN	10 mN	3 mN

As it will be shown in section 4.4, the ratio of intake area A_{intake} over total frontal area $A_{frontal}$ is central to the required performance, in terms of specific impulse and power, of the ABEP system. In case of the flat body configuration, this ratio can be increased by adding more thrusters (the same could be done for the slender body configuration, but it would thereby turn into a flat body). Tab. 16 therefore lists the effect that varying the numbers of thrusters has on the ratio $A_{intake}/A_{frontal}$ as well as on the drag coefficient for a flat body with two to eight thrusters.

Two points are notable with regard to this variation:
- Firstly, configurations with even numbers of intakes are more advantageous in terms of $A_{intake}/A_{frontal}$, which is due to the fact that in order to maintain symmetry, the odd-numbered options have a double-wide "central compartment".
- Secondly, the drag coefficient decreases with increasing number of thrusters, until it increases again with eight thrusters. This is due to the fact that with eight thrusters, the spacecraft becomes wider than it would need to be in order to accommodate the 10 m² of solar panels.

Table 16. Effect of number of thrusters of a flat body configuration on $A_{intake}/A_{frontal}$ and C_D (latter for 200 km altitude)

Thrusters	A_{intake} [m²]	$A_{intake}/A_{frontal}$	C_D ($\beta = 1$)	C_D ($\beta = 0$)
2	0.28	0.77	5.24	3.62
3	0.42	0.76	4.19	2.58
4	0.55	0.84	4.02	2.23
5	0.69	0.82	3.60	1.86
6	0.83	0.87	3.56	1.71
7	0.97	0.85	3.35	1.54
8	1.11	0.89	3.45	1.58

4.3.2.4 Comparison with "Adapted" Flat Body

The flat body configuration with the revised specular intake design features a slightly adapted spacecraft

design compared to the "original" flat body, as shortly indicated in section 4.1.3. In addition to the adapted geometry of compartments and intakes, it furthermore adapts a first measure of drag reduction: instead of deploying all solar panels towards the sides of the spacecraft, panels are also deployed towards the back of the (shortened) spacecraft body. This leads to the lower side of the panels deployed directly behind the spacecraft body being "shadowed" from the flow and therefore not contributing to drag (for a more detailed discussion of the effect compare e.g. [50]). The geometric dimensions of this configuration are shown in Tab. 17.

Table 17. Geometric dimensions of "adapted" flat body with shortened specular intakes

Number of intakes	6
Spacecraft body	1.55 m
Spacecraft height	0.32 m
Central body width	1.97 m
Deployable solar panel width (each side)	0.97 m
Deployable solar panel thickness	0.01 m
Length of deployed solar panels behind main body	1.0 m
Specular intake diameter	0.30 m
Full frontal area	0.52 m²
Intake area	0.42 m²

Again, for a flight altitude of 200 km, the drag coefficient of this configuration was found to be 4.29 for $\beta = 1$ and 2.57 for $\beta = 1$. Tab. 18 summarizes the corresponding drag forces at three different altitudes.

Table 18. Spacecraft drag at different altitudes for "adapted" flat body with shortened specular intakes. $F_{D,\perp}$ and $F_{D,\parallel}$ denote drag contributions from surfaces perpendicular and parallel to the flow, respectively.

	150 km	200 km	250 km
Intake fully contributing ($\beta = 1$)			
Total drag	131.6 mN	19.0 mN	5.1 mN
$F_{D,\perp}$	69.9 mN	9.4 mN	2.4 mN
$F_{D,\parallel}$	61.7 mN	9.6 mN	2.7 mN
Intake not contributing ($\beta = 0$)			
Total drag	75.5 mN	11.4 mN	3.3 mN
$F_{D,\perp}$	13.7 mN	1.8 mN	0.5 mN
$F_{D,\parallel}$	61.7 mN	9.6 mN	2.7 mN

It is notable that the overall drag, and both contributions from surfaces perpendicular and parallel to the flow are lower than in case of the "original" flat body. In case of $F_{D,\perp}$, this is simply due to both the frontal area of the intakes and the rest of the frontal area of the spacecraft (the spacecraft height is smaller by around ¼) being smaller than for the "original" small body. In case of $F_{D,\parallel}$, this is due to additional surface areas contributed by the additional intakes, but decreases due to the smaller

height of the spacecraft and the abovementioned "shadowing" of part of the solar panels.

4.3.2.5 Possibilities to Reduce Drag

It should be noted that neither the simplified slender body nor the simplified flat body configurations are optimized for minimal drag. Also in case of the "adapted" flat body, only one simple drag reduction measure was taken. In a more detailed analysis in a next design step, several measures can be taken in order to reduce drag and optimize the shapes, particularly including:

- An optimization of the front geometry (e.g. slanting) [38] to reduce drag of perpendicular areas;
- In combination with the mass distribution, it may be beneficial to aspire aerostability in order to avoid large aerodynamic disturbance torques.
- Such steps will need to be undertaken for either configuration that was to be studied further.

4.4 ABEP Performance Needs of Slender Body and Flat Body

The analysis of required ABEP performance, particularly in terms of total required ABEP power and required specific impulse of the thrusters, is based on the assumption that at any point of the orbit, the thrust provided by the ABEP system exactly counteracts the drag. While in case of the particular study at hand, the use of a constant altitude and constant atmospheric condition implies the assumption of constant drag and power over the orbit, the strategy as well as the following calculation can also be used for more detailed analyses with variable atmospheric conditions and for different orbit types.

The thrust provided by the ABEP system is thereby fundamentally, depending on the mass flow $\dot{m}_{thr}$ and the exhaust velocity c_e of the accelerated particles,

$$T = \dot{m}_{thr}\, c_e \qquad (6)$$

Assuming no loss of mass flow in the thruster, the exiting mass flow is thereby equal to the collected mass flow

$$\dot{m}_{thr} = \rho\, A_{intake}\, v\, \eta_c \qquad (7)$$

With $T = F_D$ and

$$F_D = \frac{1}{2}\, \rho\, C_D\, A_{frontal}\, v^2 \qquad (8)$$

(using the total spacecraft drag coefficient according to equation (5)), it follows that the required exhaust velocity is

$$c_e = \frac{1}{2}\frac{A_{frontal}}{A_{intake}\eta_c}\, v\, C_D \qquad (9)$$

And, with g being the gravitational acceleration, the required specific impulse is

$$I_{SP} = \frac{1}{2}\frac{v}{g}\frac{A_{frontal}}{A_{intake}\eta_c}C_D \qquad (10)$$

By inserting the required specific impulse (equation 9) and the collected mass flow (equation 7) into the description of the jet power

$$P_{jet} = \frac{1}{2}\dot{m}_{thr}c_e^2 \qquad (11)$$

And accounting for the thruster efficiency η_T, the required total ABEP power for full drag compensation follows to be

$$P_{ABEP} = \frac{1}{8}\rho(h)v^3(h)\,A_{frontal}^2 C_D^2\,\frac{1}{A_{intake}\eta_c\eta_T} \qquad (12)$$

Here, $v(h)$ is the spacecraft velocity, g the gravitational acceleration, η_c the intake efficiency, and η_T the thruster efficiency.

4.4.1 I_{SP} Requirements of Different Flat Body Configurations

As, for the flat body configuration, the number of thrusters makes a large difference in terms of $A_{intake}/A_{frontal}$, first the required weight-specific impulse of different flat body configurations is compared. Note that in line with Eq.3, the required specific impulse is mostly independent of altitude. Fig. 20 thus compares the required specific impulse for flat body spacecraft with different numbers of intakes, from $\beta = 0$ to $\beta = 1$.

In order to be conservative and to keep the requirement on the I_{SP} provided by the thruster relatively small, a configuration with six intakes is used for the following comparison in between slender and flat body configurations.
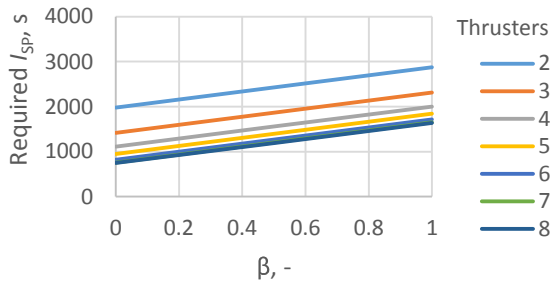
Figure 20. Comparison of required specific impulse I_{SP} of ABEP thruster for flat body configurations with different numbers of thrusters + intakes

4.4.2 I_{SP} and Power Requirements of Slender and Flat Body Configurations

Fig. 21 shows the required specific impulse for full drag compensation for the three different configurations over the full range of potential values of β.

It becomes obvious that for any value of β, the flat body configuration with its high $A_{intake}/A_{frontal}$, combined with the high intake efficiency of the specular intake, is advantageous over the slender body configuration.
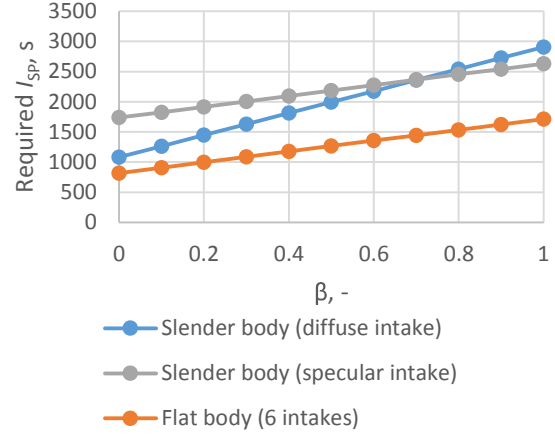
Figure 21. Required specific impulse I_{SP} for full drag compensation for different configurations.

It is furthermore interesting to note that the slender body configuration with a specular intake, due to the limited possible size of the intake (see Tab. 2) and the therefore limited $A_{intake}/A_{frontal}$, is disadvantageous when comparing it to the configuration with diffuse intake over a wide range of β.

Fig. 22 extends the comparison to the required total ABEP power (in case of the flat body, over all thrusters). This consideration equally shows that for any value of β, the flat body configuration is advantageous over the slender body configuration. The power values provided here refer to power at the ABEP thrusters, i.e. they do not consider the efficiency of the power processing unit.
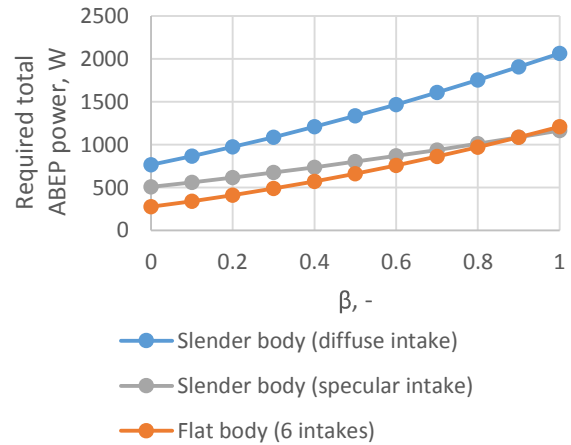
Figure 22. Required total (all thrusters) ABEP power for full drag compensation at 200 km altitude for different configurations.

4.4.3 Comparison with Flat Body Adapted to Specular Intake Limitations

The abovementioned configurations with specular intakes could be regarded as theoretical optima if the particle flow in VLEO could be treated as being parallel.
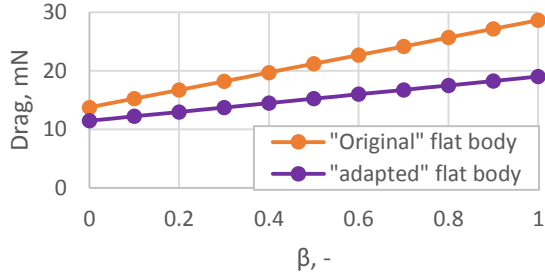

Figure 23. Comparison between total spacecraft drag of "original" and "adapted" flat body design (both with 6 intakes) at 200 km altitude.

Fig. 24 therefore shows the mass specific impulse for the adapted configuration plotted over the required mass specific impulse of the aforementioned configurations. It is immediately evident that, as the smaller diameter intakes as well as the reduced intake efficiency decrease the mass flow arriving at the thrusters, the required I_{SP} is considerably higher than that of the "original" flat body configuration. Although reaching the limit of the above set I_{SP} range, preliminary results from performance characterization of the thruster are optimistic and suggest values exceeding 3000 s. A publication of these data is planned. Fig. 25 complements the comparison with regard to required ABEP power. The comparison shows a significant increase in the required ABEP power as compared to the "original" flat body design, particularly for low β-values, and a similar requirement as compared to the "original" slender body design with a specular intake. The decrease in difference compared to the "original" flat body towards high β-values is due to larger intakes of the "original" flat body (42 cm diameter vs. approx. 30 cm), which lead to a higher drag at high β-values, see also Fig. 23. The required ABEP power remains, however, significantly below that required for a slender body with a diffuse intake.

In order to allow for a first glimpse of whether the design loop may close, we also indicate in Fig. 23 the roughly estimated average available power over the orbit that could be provided by 10 m² of solar panels (assuming a cell efficiency of 31.8 %, total losses of 65.1 % on part of the panels, a cosine factor of 0.6366, panels only being illuminated for 50 % of the orbit and power conversion and storage losses of 76 % during "day", 55 % during night; all losses noted as "efficiencies"; not taking into account ageing of solar cells and power usage by other subsystems).
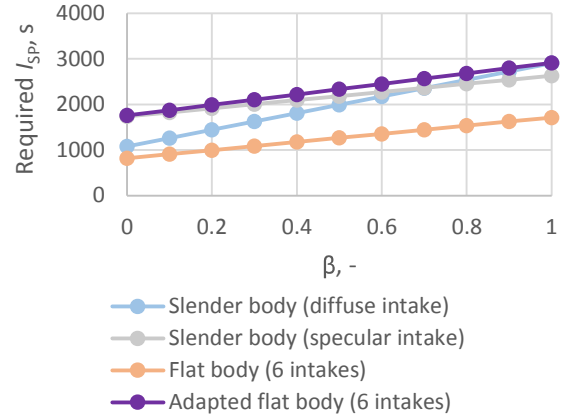

Figure 24. Required specific impulse I_{SP} of adapted flat body design (taking into account thermal movement of particles).

Drawing definite conclusions from this comparison remains difficult. Given the current knowledge, the "original" slender and flat body configurations should at most be treated as reference scenarios for "perfect" intake designs. The comparison between the adapted flat body and the slender body with diffuse intakes is complicated by the fact that the same solar panel area was used in both cases, while the power requirement clearly indicates that the slender body with diffuse intake will require considerably more power. In addition, β is still unknown and may differ considerably between the diffuse and the specular intakes.

Work on a more detailed system model and on determining β, which will allow a better comparison, is currently ongoing.
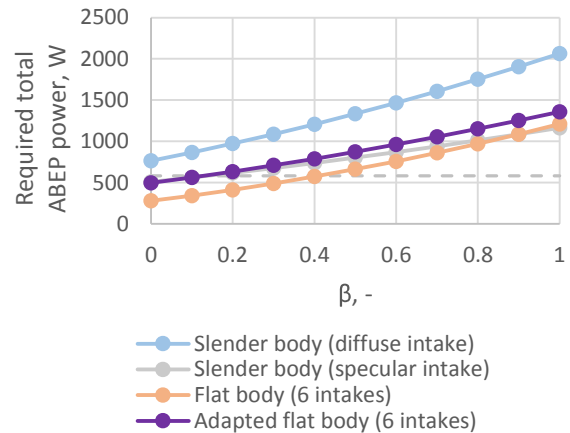

Figure 25. Required total ABEP power (all thrusters) of adapted flat body design (taking into account thermal movement of particles) at 200 km altitude. Dashed grey line indicates (rough) average power available from 10 m² solar panels.

4.5 Limitations of the analysis

As already indicated above, the analysis presented is limited in several ways:

- The solar panel area was assumed to be the same (10 m²) for all configurations,
- The β–value is unknown for diffuse intakes.
- Recent PICLas simulations lead to β–values for diffuse intakes, showing a variation over altitude [43]. Due to the early nature of these analyses, they were not considered in the analysis at hand, however.
- The spacecraft designs were not optimized for drag reduction.

5. Conclusions and Outlook

The characterization testing activities of the RF-based Helicon Plasma Thruster have been initiated. A torsional pendulum to measure the momentum flux and a 3-axes B-dot probe to evaluate the discharge behaviour of the IPT were developed. Calibration set-ups were built for both probes. The MFP probe has undergone a calibration process and the calibration curves were extracted. The MFP was functionally checked, using both a cold gas flow and a plasma flow. While the movement of the probe has been identified during IPT operation, further experiments are ongoing to measure the thrust of the plasma plume. The extracted data will be used to derive important parameters such as specific impulse and thrust efficiency.

A system analysis was conducted on platform level, comparing two different spacecraft configurations with "idealized" atmospheric intakes. The two configurations were compared to a configuration with an intake simulated under hypothermal flow.

In the idealized cases, a flat body configuration showed advantages in terms of specific impulse and overall power consumption over a slender body configuration. However, the comparison with the intake analysed under hypothermal flow and with a spacecraft design adapted accordingly showed significantly higher performance requirements for the ABEP system. One of the central conclusions of this analysis is therefore that, particularly for the design and assessment of specular intakes, the particle flow in VLEO cannot be treated as being hyperthermal without running the risk of gravely misjudging the intake performance. An implication of this analysis is that the current, paraboloid design for specularly reflecting intakes, which is optimized for a parallel flow of particles, may not be the optimum shape for realistically expectable flow conditions.

In order to conclude on the viability of the studied spacecraft configurations, further work is required. Several activities in this direction are therefore still ongoing under the Ram-CLEP project. These include the continued study of specular intake designs and their contributions to drag with DSMC simulations using PICLas as well as studies on the spacecraft design using a multi-disciplinary optimization of the full spacecraft system. The results will provide valuable insights into the feasibility of the studied system.

References

[1] N.H. Crisp, P.C.E. Roberts, S. Livadiotti, V.T.A. Oiko, S. Edmondson, S.J. Haigh et al., The Benefits of Very Low Earth Orbit for Earth Observation Missions, Progress in Aerospace Sciences 117 (2020).

[2] S. Vaidya, C. Traub, F. Romano, G. Herdrich, Y.-A. Chan, S. Fasoulas et al., Development and analysis of novel mission scenarios based on Atmosphere-Breathing Electric Propulsion (ABEP), CEAS Space Journal (2022).

[3] A.S. Filatyev, A.A. Golikov, A.I. Erofeev, S.A. Khartov, A.S. Lovtsov, D.I. Padalitsa et al., Research and development of aerospace vehicles with air breathing electric propulsion: Yesterday, today, and tomorrow, Progress in Aerospace Sciences 136 (2023) 100877.

[4] P. Zheng, J. Wu, Y. Zhang, B. Wu, A Comprehensive Review of Atmosphere-Breathing Electric Propulsion Systems, International Journal of Aerospace Engineering 2020 (2020).

[5] J. Wu, P. Zheng, Y. Zhang, H. Tang, Recent development of intake devices for atmosphere-breathing electric propulsion system, Progress in Aerospace Sciences 133 (2022) 100848.

[6] K.D. Diamant, Microwave Cathode for Air Breathing Electric Propulsion, in: 31st International Electric Propulsion Conference, Ann Arbor, Michigan • USA: IEPC-2009-015, 2009.

[7] A. Shabshelowitz, Study of RF Plasma Technology Applied to Air-Breathing Electric Propulsion, Ph.D. Thesis, Ann Arbor, Michigan, USA, 2013.

[8] M. Tagawa, K. Yokota, K. Nishiyama, H. Kuninaka, Y. Yoshizawa, D. Yamamoto et al., Experimental Study of Air Breathing Ion Engine

Using Laser Detonation Beam Source, Journal of Propulsion and Power 29 (2013) 501–506.

[9] V. Hruby, B. Pote, T. Brogan, K. Hohmann, J. Szabo, P. Rostler, Air breathing electrically powered hall effect thruster(US6834492B2).

[10] G. Cifali, T. Misuri, P. Rossetti, M. Andrenucci, D. Valentian, D. Feili et al., Experimental characterization of HET and RIT with atmospheric propellants, in: 32nd International Electric Propulsion Conference, Wiesbaden, Germany: IEPC-2011-224, 2011.

[11] E. Ferrato, V. Giannetti, A. Piragino, M. Andrenucci, T. Andreussi, C.A. Paissoni, Development roadmap of SITAEL's RAM-EP system, in: 36th International Electric Propulsion Conference, Vienna, Austria: IEPC-2019-886, 2019.

[12] A.S. Filatyev, O.V. Yanova, The control optimization of low-orbit spacecraft with electric ramjet, Acta Astronautica 158 (2019) 23–31.

[13] E. Ahedo, P. Fajardo, M. Merino, J. Navarro-Cavalle, A. Sanchez-Villar, M. Wijnen et al., Helicon and ECR plasma sources for space propulsion: simulation and testing, in: 2019 International Conference on Electromagnetics in Advanced Applications (ICEAA), Granada, Spain, 2019, pp. 788–793.

[14] M. Ruiz, A. Velasco, V. Gómez, J. Navarro-Cavallé, G. Dickeli, A. Vinci et al., Results of the first Helicon Plasma Thruster (HPT) coupling test campaign within the HIPATIA project, IEPC-2022-524, in: 37th International Electric Propulsion Conference, Cambridge, MA USA, 2022.

[15] M. Manente, F. Trezzolani, M. Magarotto, E. Fantino, A. Selmo, N. Bellomo et al., REGULUS: A propulsion platform to boost small satellite missions, Acta Astronautica 157 (2019) 241–249.

[16] P.C.E. Roberts, N.H. Crisp, S. Edmondson, S. Haigh, E.A. Brandon, B. Holmes et al., DISCOVERER: Developing Technologies to Enable Commercial Satellite Operations in Very Low Earth Orbit, in: 71st International Astronautical Congress (IAC) - The CyberSpace Edition, 2020.

[17] F. Romano, Y.-A. Chan, G. Herdrich, C. Traub, S. Fasoulas, P.C.E. Roberts et al., RF Helicon-based Inductive Plasma Thruster (IPT) Design for an Atmosphere-Breathing Electric Propulsion system (ABEP), Acta Astronautica 176 (2020) 476–483.

[18] F. Romano, G. Herdrich, Y.-A. Chan, N. Crisp, P.C.E. Roberts, B.E.A. Holmes et al., Design of an intake and a thruster for an atmosphere-breathing electric propulsion system, CEAS Space Journal 14 (2022) 707–715.

[19] F. Romano, RF Helicon Plasma Thruster for an Atmosphere-Breathing Electric Propulsion System (ABEP), Dr. Hut, München, 2022.

[20] S. Rodriguez-Donaire, M. Sureda, D. Garcia-Almiñana, E. Sierra, J. S. Perez, P. C.E. Roberts et al., Earth Observation Technologies: Low-End-Market Disruptive Innovation, in: V. Demyanov, J. Becedas (Eds.), Satellites Missions and Technologies for Geosciences, IntechOpen, 2020.

[21] L. Berthoud, R. Hills, A. Bacon, M. Havouzaris-Waller, K. Hayward, J.-D. Gayrard et al., Are Very Low Earth Orbit (VLEO) satellites a solution for tomorrow's telecommunication needs?, CEAS Space J 14 (2022) 609–623.

[22] M. Borowitz, The Military Use of Small Satellites in Orbit, Briefings de l'Ifri, Ifri, ISBN: 979-10-373-0499-5, 2022.

[23] A. Bacon, B. Olivier, Skimsats: bringing down the cost of Earth Observation, in: S. Hatton (Ed.), Proceedings of the 12th Reinventing Space Conference, Springer International Publishing, Cham, 2017, pp. 1–7.

[24] Jacquier R., R. Agnello, B.P. Duteil, P. Guittienne, A. Howling, G. Plyushchev et al., First B-dot measurements in the RAID device, an alternative negative ion source for demo neutral beams, Fusion Engineering and Design 146 (2019) 1140–1144.

[25] P. Guittienne, R. Jacquier, B. Pouradier Duteil, A.A. Howling, R. Agnello, I. Furno, Helicon wave plasma generated by a resonant birdcage antenna: magnetic field measurements and analysis in the RAID linear device, Plasma Sources Sci. Technol. 30 (2021) 75023.

[26] M. Silvia, F. Romano, R. Soglia, Herdrich Georg, P. Roberts, T. Schönherr et al., Analysis of electrodeless plasma source enhancement by an externally applied magnetic field for an inductive plasma thruster (IPT), in: 7th Russian-German Conference on Electric Propulsions and Their Application, Rauischholzhausen, Germany, 2018.

[27] Schafft Marcel, Design and Test of a Baffle Plate to Perfom First Thrust Measurement of the IPT: IRS-22-S-008, Master Thesis, Institute of Space Systems, University of Stuttgart, 2022.

[28] K. Takahashi, Helicon-type radiofrequency plasma thrusters and magnetic plasma nozzles, Reviews of Modern Plasma Physics 3 (2019).

[29] L.D. Flansburg, N. Hershkowitz, Magnetism in Austenitic Stainless Steels, Journal Article in Journal of Applied Physics 41 (1970).

[30] K. Takahashi, A. Komuro, A. Ando, Measurement of plasma momentum exerted on target by a small helicon plasma thruster and comparison with direct thrust measurement, Review of Scientific Instruments 86 (2015).

[31] G. Herdrich, J. Skalden, A. Behnke, F. Schäfer, Z. Zhang, K. Papavramidis et al., An Overview of Recent Thrust Balance Developments at the Institute of Space Systems, IEPC-2022-167, in: 37th International Electric Propulsion Conference, Cambridge, MA USA, 2022.

[32] K. Papavramidis, J. Skalden, N. Souhair, G. Herdrich, P. Maier, S. Klinkner et al., Development Activities for the RF Helicon-based Plasma Thruster: Thrust Measurement and B-dot Probe Set-up, IEPC-2022-167, in: 37th International Electric Propulsion Conference, Cambridge, MA USA, 2022.

[33] W.A. Johnson, L.K. Warne, Electrophysics of micromechanical comb actuators, IEEE∨ASME Journal of Microelectromechanical Systems 4 (1995) 49–59.

[34] A. Spethmann, T. Trottenberg, H. Kersten, F.G. Hey, L. Grimaud, S. Mazouffre et al., Force probes for development and testing of different electric propulsion systems, EPJ Techn Instrum 9 (2022).

[35] T. Trottenberg, A. Spethmann, H. Kersten, An interferometric force probe for beam diagnostics and the study of sputtering, Physics of Plasmas 24 (2017).

[36] K.A. Polzin, C.S. Hill, P.J. Turchi, R.L. Burton, S. Messer, R.H. Lovberg et al., Recommended practice for use of inductive magnetic field probes in electric propulsion testing, Journal of Propulsion and Power 33 (2017) 659–667.

[37] S. Bose, M. Kaur, K.K. Barada, J. Ghosh, P.K. Chattopadhyay, R. Pal, Understanding the working of a B-dot probe, European Journal of Physics 40 (2018).

[38] E.T. Everson, P. Pribyl, C.G. Constantin, A. Zylstra, D. Schaeffer, N.L. Kugland et al., Design, construction, and calibration of a three-axis, high-frequency magnetic probe (B-dot probe) as a diagnostic for exploding plasmas, Review of Scientific Instruments 80 (2009).

[39] F. Romano, J. Espinosa-Orozco, M. Pfeiffer, G. Herdrich, N.H. Crisp, P.C.E. Roberts et al., Intake design for an Atmosphere-Breathing Electric Propulsion System (ABEP), Acta Astronautica 187 (2021) 225–235.

[40] F. Romano, T. Binder, G. Herdrich, S. Fasoulas, Air-Intake Design Investigation for an Air-Breathing Electric Propulsion System, in: 34th International Electric Propulsion Conference, Hyogo-Kobe, Japan, 2015.

[41] S. Fasoulas, C.D. Munz, M. Pfeiffer, J. Beyer, T. Binder, S. Copplestone et al., Combining particle-in-cell and direct simulation Monte Carlo for the simulation of reactive plasma flows, Physics of Fluids 31 (2019) 72006.

[42] V.J. Murray, M.D. Pilinski, E.J. Smoll, M. Qian, T.K. Minton, S.M. Madzunkov et al., Gas-Surface Scattering Dynamics Applied to Concentration of Gases for Mass Spectrometry in Tenuous Atmospheres, Journal of Physical Chemistry C 121 (2017) 7903–7922.

[43] K. Feng, Investigation of a Novel Atmosphere-Breathing Electric Propulsion Platform and Intake, Master Thesis, KTH Royal Institute of Technology, 2023.

[44] K. Takahashi, Thirty percent conversion efficiency from radiofrequency power to thrust energy in a magnetic nozzle plasma thruster, Scientific reports 12 (2022) 18618.

[45] M.R. Drinkwater, R. Haagmans, D. Muzi, A. Popescu, R. Floberghagen, M. Kern et al., The GOCE Gravity Mission: ESA's First Core Earth Explorer, in: Proceedings of 3rd International GOCE User Workshop, 2007, pp. 1–8.

[46] F. Hild, C. Traub, M. Pfeiffer, J. Beyer, S. Fasoulas, Optimisation of satellite geometries in Very Low Earth Orbits for drag minimisation and lifetime extension, Acta Astronautica 201 (2022) 340–352.

[47] M.A.M. Serrano, D. Kuijper, J. Sánchez, P. Ramos-Bosch, D. Sieg, GOCE FLIGHT DYNAMICS SUPPORT TO THE LOW ORBIT AND DEORBITING OPERATIONS, in: 24th International Symposium on Space Flight Dynamics, Laurel, Maryland, USA, 2014.

[48] D. Di Cara, J. Del Gonzalez Amo, A. Santovincenzo, B. Carnicero Dominguez, M. Arcioni, A. Caldwell et al., RAM Electric Propulsion for Low Earth Orbit Operation: an ESA study, in: 30th International Electric Propulsion Conference, Florence, Italy, 2007.

[49] T. Schönherr, K. Komurasaki, F. Romano, B. Massuti-Ballester, G. Herdrich, Analysis of atmosphere-breathing electric propulsion, IEEE Transactions on Plasma Science 43 (2015) 287–294.

[50] L.H. Sentman, Free molecular flow theory and its application to the determination of aerodynamic forces, Sunnyvale, 1961.

[51] L.A. Sinpetru, N.H. Crisp, D. Mostaza-Prieto, S. Livadiotti, P.C.E. Roberts, ADBSat: Methodology of a novel panel method tool for aerodynamic analysis of satellites, Computer Physics Communications 275 (2022) 108326.